

Article

# Two-Dimensional Fe-N-C Nanosheets for Efficient Oxygen Reduction Reaction

Xin Wu <sup>1</sup>, Wenke Xie <sup>1</sup>, Xuanhe Liu <sup>1,\*</sup>, Xiaoming Liu <sup>1,\*</sup>  and Qinglan Zhao <sup>2,\*</sup><sup>1</sup> School of Science, China University of Geosciences (Beijing), Beijing 100083, China<sup>2</sup> Department of Chemical and Biological Engineering, The Hong Kong University of Science and Technology, Clear Water Bay, Kowloon, Hong Kong 999077, China

\* Correspondence: liuxh@cugb.edu.cn (X.L.); xmliu@mail.nwpu.edu.cn (X.L.); keqzhao@ust.hk (Q.Z.)

**Abstract:** Fe-N-doped carbon (Fe-N-C)-based electrocatalysts are considered to be promising alternatives to replace Pt-based catalysts for oxygen reduction reactions (ORR). Here, we reported a simple and effective approach to prepare Fe-N-C-based electrocatalysts with the shape of two-dimensional nanosheets (termed Fe/NCNSs) to enhance the ORR performance. Fe/NCNSs were prepared by the calcination of Fe/Zn dual-metal ZIFs nanosheets as precursors. Benefiting from its higher specific surface area, electrochemically active surface area, and proportion of pyridinic N and Fe-N, the optimized Fe/NCNS showed excellent ORR performance both in acidic ( $E_{1/2} = 0.725$  V vs. RHE) and alkaline ( $E_{1/2} = 0.865$  vs. RHE) media, being 23 mV more negative and 24 mV more positive than that of a commercial Pt/C. The optimized Fe/NCNS also exhibited long durability. In addition, the Zn-air battery with Fe/NCNS-1 and RuO<sub>2</sub> as the air catalyst exhibited high power density (1590 mW cm<sup>-2</sup> at a current density of 2250 mA cm<sup>-2</sup>) and superior charging/discharging durability.

**Keywords:** oxygen reduction reaction; electrocatalysts; ZIFs; Fe-N-C

**Citation:** Wu, X.; Xie, W.; Liu, X.; Liu, X.; Zhao, Q. Two-Dimensional Fe-N-C Nanosheets for Efficient Oxygen Reduction Reaction. *Catalysts* **2022**, *12*, 1276. <https://doi.org/10.3390/catal12101276>

Academic Editors: Yu Zhang, Yao Yao and Mengjiao Wang

Received: 21 September 2022

Accepted: 17 October 2022

Published: 19 October 2022

**Publisher's Note:** MDPI stays neutral with regard to jurisdictional claims in published maps and institutional affiliations.



**Copyright:** © 2022 by the authors. Licensee MDPI, Basel, Switzerland. This article is an open access article distributed under the terms and conditions of the Creative Commons Attribution (CC BY) license (<https://creativecommons.org/licenses/by/4.0/>).

## 1. Introduction

Zinc-air batteries (ZABs) are a next-generation promising energy conversion technology due to their high energy conversion efficiency, low-cost and environmentally friendly characteristics [1–3]. Nevertheless, the sluggish kinetics of the oxygen reduction reaction (ORR) at the cathode limits their development [4–7]. Though Pt-based materials have proved to be effective catalysts, their commercialization is impeded by their high cost, poor methanol tolerance and CO deactivation. Therefore, there is an urgent need to explore efficient and low-cost nonprecious metal catalysts (NPMCs) to replace Pt. Among NPMCs, Fe-N-doped carbon (Fe-N-C, N, nitrogen, C carbon)-based electrocatalysts are of considerable interest due to their promising performance in ORR. Despite the progress made, Fe-N-C-based electrocatalysts still need further development to take the place of commercial Pt electrocatalysts, especially in acidic media.

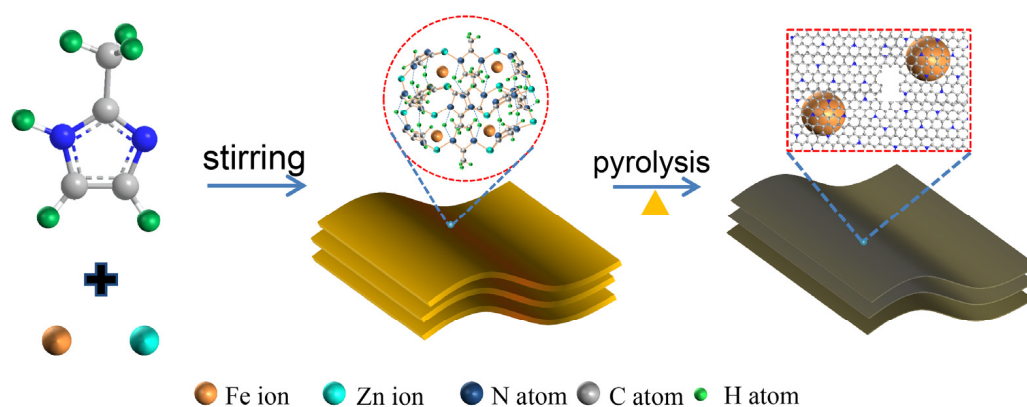
To enhance the performance of ORR for Fe-N-C-based electrocatalysts, multiple characteristics including the effective exposure of active sites, short diffusion distance for reactants to active sites and fast electron transport are pivotal. Two-dimensional carbon materials, such as graphenes or N-doped carbon nanosheets, have all the aforementioned advantages to facilitate the ORR process [8–10]. Therefore, Fe-N-C-based electrocatalysts with the shape of two-dimensional nanosheets are expected to exhibit efficient ORR performances due to their easily accessible active sites, unique electronic properties, and large specific surface areas. Zeolitic imidazolate frameworks (ZIFs) have an inherent N element and exhibit zeolite-like structural topologies and regulable morphologies with exceptional thermal and chemical stability, which are considered to be desirable precursors to fabricate porous N-doped carbon-based functional materials [11,12]. For instance, Zhang et al. [13] presented a defect-rich ultrathin Co(OH)<sub>2</sub> nanoarray by etching ZIF-L-Co—the activity is 3–4 times higher than that of the commercial RuO<sub>2</sub> and superior to that of the reported exfoliated

bimetallic catalysts. Guan et al. [14] synthesized a novel dual-metal 2D ZIF by introducing surfactant (PVP)—the derived materials exhibited a power density of  $\sim 125.41 \text{ mW}\cdot\text{cm}^{-2}$  for a Zn-air battery with an extraordinary cyclability over 673 h.

Herein, we reported a simple and effective approach to prepare Fe-N-C-based electrocatalysts with the shape of two-dimensional nanosheets (termed as Fe/NCNSs) by the calcination of Fe/Zn dual-metal ZIF-8. The optimized Fe/NCNS exhibited outstanding ORR activity and durability in both acidic and alkaline media. The half-wave potential of the optimized Fe/NCNS was 0.725 V (all potentials were vs. RHE hereinafter) in acidic media, and only 23 mV more negative than that of commercial Pt/C (0.748 V). Further, the current density still preserved about 80% of its initial current density after 120 h in an electrochemical stability test, superior to the commercial Pt/C and many other reported catalysts. Likewise, the optimized Fe/NCNS also showed an excellent ORR performance in alkaline media with a half-wave potential of 24 mV more positive than commercial Pt/C and outstanding electrochemical stability. More importantly, the rechargeable Zn-air battery using Fe/NCNS-1 as the air electrode exhibited high power density ( $1590 \text{ mW cm}^{-2}$  at a current density of  $2250 \text{ mA cm}^{-2}$ ), a low charge–discharge gap (0.63 V at  $5 \text{ mA cm}^{-2}$ ) and long-term stability (over 300 cycles at  $5 \text{ mA cm}^{-2}$ ).

## 2. Results and Discussion

The schematic synthetic route is displayed in Scheme 1. Scanning electron microscope (SEM) images in Figure S1 show that the prepared Fe/Zn-ZIFs exhibited the shape of two-dimensional nanosheets. It can be observed that the aggregation of nanosheets began to appear in Fe/Zn-ZIF-2, indicating that Fe played a role in morphology control. Fe/NCNSs maintained their shape after carbonization (Figures 1a and S1). The transmission electron microscope (TEM) image of Fe/NCNS-1 in Figure 1b further demonstrated its morphology of nanosheets. Scattered nanoparticles were found in Fe/NCNS-1. The high-resolution TEM (HRTEM) image in Figure 1c shows the lattice fringe of 0.202 nm in nanoparticles, indexed as (110) plane of cubic  $\text{Fe}^0$ , and demonstrating the Fe nanoparticles [15]. The lattice spacing of carbon sheets on the edge of Fe nanoparticles was 0.36 nm, corresponding to the (002) plane of graphitic carbon and illustrating that Fe nanoparticles were encapsulated by several layers of graphite carbon. The distortion of the fringe can be clearly observed (highlighted by a yellow circle) in Figure 2c. Structural defects have been reported to be beneficial to the electrochemical performance [16] and the distortion was expected to enhance the catalytic activities. The element distribution of Fe/NCNS-1 was investigated by energy dispersive spectrum (EDS) elemental mapping analysis. As shown in Figure 1e–i, C, N, O and Fe elements were well dispersed in Fe/NCNS-1.



**Scheme 1.** The schematic synthetic route of Fe/NCNSs.

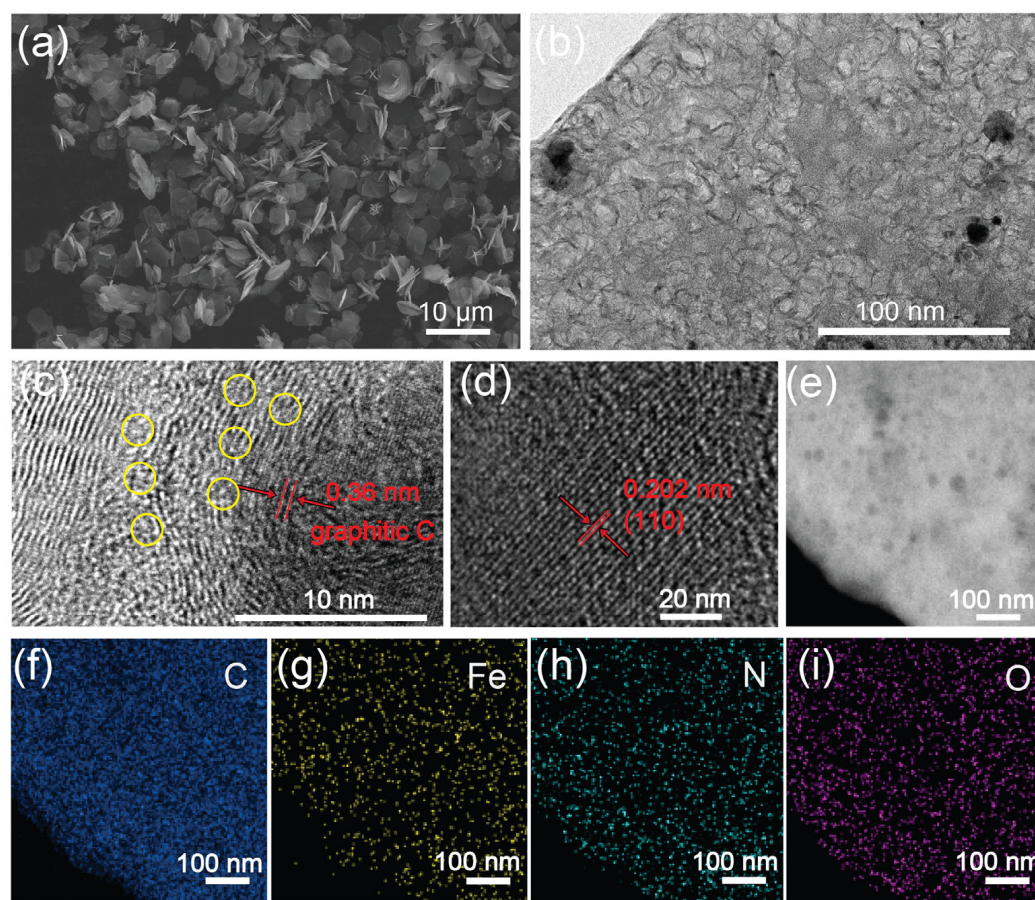


**Figure 1.** (a) SEM image of Fe/NCNS-1; (b–d) high-resolution TEM image of Fe/NCNS-1 at different magnifications; (e–i) EDS elemental mapping of Fe/NCNS-1.

X-ray powder diffraction (XRD) was performed to characterize their composition and chemical phase. As shown in Figure S2, Fe/Zn-ZIFs showed similar XRD patterns, indicating that  $\text{Fe}^{3+}$  was absorbed on the surface of ZIFs or captured in the cavities [17]. XRD patterns of Fe/NCNSs in Figure 2a display that Fe/NCNSs exhibited two distinct broad peaks at around  $26^\circ$  and  $44^\circ$ , indexed as (002) and (101) planes of partially graphitized carbon [18,19]. In the XRD pattern of Fe/NCNS-2, diffraction peaks at  $44.8^\circ$  and  $82.3^\circ$  were ascribed to (110) and (211) planes of metallic Fe, and others corresponded to  $\text{Fe}_3\text{C}$  (JCPDS No. 35-0772) [20]. No obvious peaks relating to metallic Fe or  $\text{Fe}_3\text{C}$  were observed in the XRD pattern of Fe/NCNS-1, indicating that only a small amount of metallic Fe or  $\text{Fe}_3\text{C}$  formed in Fe/NCNS-1. Raman spectra of Fe/NCNSs are displayed in Figure 2b. The  $I_D/I_G$  values of Fe/NCNS-0, Fe/NCNS-1 and Fe/NCNS-2 were 1.28, 1.25 and 1.24, respectively, demonstrating their similar carbon structure.

$\text{N}_2$  adsorption–desorption isotherms were used to investigate their specific surface area and pore size distribution. Figure 2c depicts the characteristics of combined type II and type IV isotherms, indicating the existence of micropores and mesopores [21]. The surface areas of Fe/NCNS-0, Fe/NCNS-1 and Fe/NCNS-2 were  $780.9$ ,  $740.4$ , and  $329.9 \text{ m}^2 \cdot \text{g}^{-1}$ , respectively. It can be concluded that Fe not only played a role in morphology control but also regulated the surface area of Fe/NCNS. The pore size distribution of Fe/NCNSs mainly peaked at 1.7, 3.9 and 13.3 nm (Figure 2d), further demonstrating the co-existence of micropores and mesopores. Compared with Fe/NCNS-0 and Fe/NCNS-2, Fe/NCNS-1 exhibited more mesopores, which were expected to offer more active sites [22].

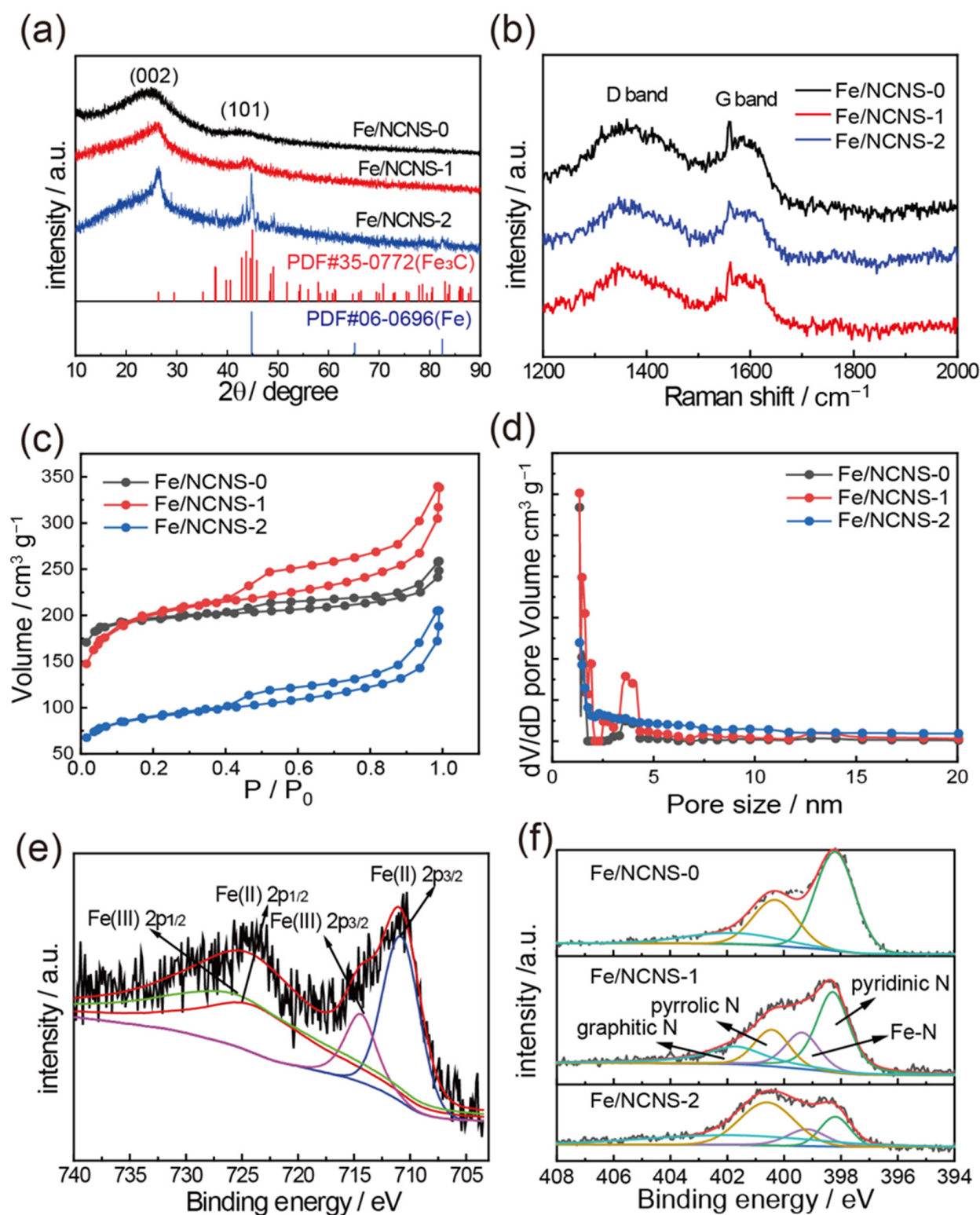


**Figure 2.** (a) XRD patterns, (b) Raman spectrum spectra (c)  $N_2$  adsorption-desorption isotherms, (d) pore size distribution of Fe/NCNS-0, Fe/NCNS-1 and Fe/NCNS-2, (e) Fe 2p spectra of Fe/NCNS-1, (f) N 1s spectra of Fe/NCNS-0, Fe/NCNS-1 and Fe/NCNS-2.

The X-ray photoelectron spectroscopy (XPS) survey spectra of Fe/NCNSs in Figure S3 demonstrated the C 1s, N 1s, O 1s and Fe 2p peaks without other signals. Figure 2e gives the high-resolution Fe 2p spectrum. The peaks at 710.8 and 725.4 eV were attributed to Fe 2p<sub>3/2</sub> and 2p<sub>1/2</sub> of Fe<sup>2+</sup>. Further, the binding energies of 714.4 and 732.8 eV were ascribed

to Fe 2p<sub>3/2</sub> and Fe 2p<sub>1/2</sub> of Fe<sup>3+</sup>, respectively [21]. No Fe<sup>0</sup> peak can be found in the split Fe 2p spectrum, probably due to the thick carbon layers covering the small Fe particles [23]. In Figure S3, the O 1s spectra of Fe/NCNSs can be split into two deconvoluted bands at 531.8 and 533.3 eV which are assigned to O-C and O-C=O, respectively [24]. For C 1s spectra, three deconvoluted peaks at 284.4, 285.5 and 286.7 eV can be attributed to C-C, C-N and C=O, respectively [25]. In Figure 2f, N 1s spectra of Fe/NCNS-1 and Fe NCNS-2 were deconvoluted into four peaks at 398.8, 399.9, 400.7 and 401.7 eV assigned to pyridinic N, Fe-N, pyrrolic N and graphitic N, respectively [19,26]. N 1s spectra of Fe/NCNS-0 showed deconvoluted peaks of pyridinic N, pyrrolic N and graphitic N. Fe/NCNS-1 possessed a higher proportion of pyridinic N and Fe-N compared to Fe/NCNS-2, which would favor the ORR performance [27].

The ORR performance of Fe/NCNSs was first investigated in 0.5 M H<sub>2</sub>SO<sub>4</sub> solution. The cyclic voltammetry (CV) curves of Fe/NCNSs are shown in Figure S4. No distinct characteristic peaks were observed in the CV curves of Fe/NCNSs in the N<sub>2</sub>-saturated electrolyte, while the CV curves in the O<sub>2</sub>-saturated electrolyte all exhibited obvious cathodic peaks, illustrating their ORR performance. The positive cathodic peak of Fe/NCNS-1 suggested that Fe/NCNS-1 would be the best catalyst in ORR. The linear sweep voltammogram (LSV) curves and the comparison of half-wave potential and j<sub>K</sub> at 0.85 V are displayed in Figure 3a,b. The half-wave potential of Fe/NCNS-0-, Fe/NCNS-1- and Fe/NCNS-2-modified electrodes were 0.429, 0.725, and 0.718 V, respectively. Fe/NCNS-1 displayed the most positive half-wave potential and was only 23 mV more negative than that of commercial Pt/C (0.748 V). Moreover, Fe/NCNS-1 displayed a similar kinetic current density (j<sub>K</sub>) (3.0 mA·cm<sup>-2</sup>) to that of Pt/C (3.1 mA·cm<sup>-2</sup>) at 0.85 V, indicating its superior ORR performance. The excellent catalytic performance in acidic media outperformed many other reported catalysts (Table S1). The electrochemically active surface areas (ECSAs) of Fe/NCNSs were investigated to evaluate their electrochemical activity. Figure S5 shows the CV curves at the different scanning rates of 5, 10, 20, 30, 40 and 50 mV·s<sup>-1</sup> and the corresponding correlation between the current density at 1.81 V and the scan rate. The electrochemical capacitance (C<sub>dl</sub>) was calculated to be 7.6, 22.1, and 9.3 mF·cm<sup>-2</sup>, respectively, demonstrating the highest ECSA of Fe/NCNS-1.

To further investigate the electron transfer pathway and H<sub>2</sub>O<sub>2</sub> yield, the rotating ring disk electrode (RRDE) technique was employed (Figure 3c). The electron transfer number (n) was calculated to be 3.87, 3.98 and 3.96 for Fe/NCNS-0, Fe/NCNS-1 and Fe/NCNS-2, respectively, indicating their 4-electron-dominated electron transfer path. H<sub>2</sub>O<sub>2</sub> yield was 2.4% for Fe/NCNS-1 and 6.5% and 4.3% for Fe/NCNS-0 and Fe/NCNS-2, respectively. The ideal n value of Fe/NCNS-1 and the lower hydrogen peroxide yield for Fe/NCNS-1 disclosed its best catalytic activity in ORR. The ORR kinetics of Fe/NCNSs are further studied by calculating their Tafel slopes (Figure 3d). The Tafel slope values for Fe/NCNS-0, Fe/NCNS-1 and Fe/NCNS-2 and commercial Pt/C were 376, 115, 127, and 101 mV·dec<sup>-1</sup>, respectively, indicating that Fe/NCNS-1 exhibited a similar kinetic rate to the commercial Pt/C during ORR. The comparable performance of Fe/NCNS-1 to commercial Pt/C in ORR was attributed to its higher specific surface area, ECSA and proportion of pyridinic N and Fe-N.

Moreover, the tolerance to methanol (1 M CH<sub>3</sub>OH) (Figure 3e) and electrochemical stability (Figure 3f) were investigated by chronogalvanometry. Almost no obvious change in the current density was observed for Fe/NCNS-1 after adding methanol into the acidic solution, showing its superior tolerance to methanol compared with the commercial Pt/C. After the electrochemical stability test for 120 h, the current density still preserved about 80% of its initial current density, outperforming many other catalysts reported to date in an acidic electrolyte [28–30].

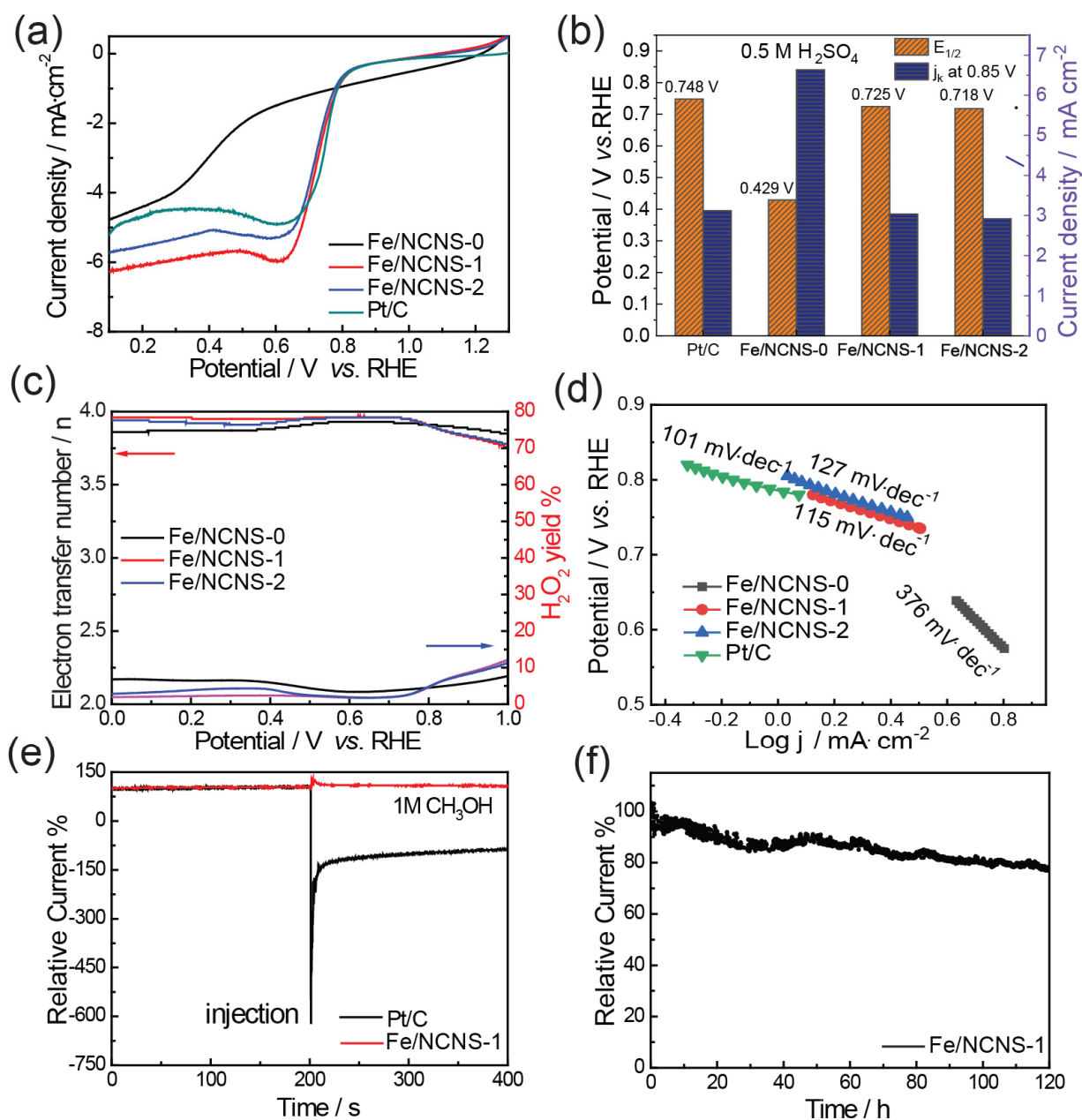


**Figure 3.** (a) LSV curves of Fe/NCNS-0, Fe/NCNS-1, Fe/NCNS-2 and commercial Pt/C at 1600 rpm·min<sup>-1</sup> in 0.5 M H<sub>2</sub>SO<sub>4</sub>, (b) comparison of  $j_k$  at 0.85 V and  $E_{1/2}$  of Fe/NCNS-0, Fe/NCNS-1, Fe/NCNS-2 and commercial Pt/C, (c) electron transfer number ( $n$ ) and the yield of H<sub>2</sub>O<sub>2</sub>; (d) Tafel plots of Fe/NCNS-0, Fe/NCNS-1, Fe/NCNS-2 and commercial Pt/C, (e) the tolerance to methanol of Fe/NCNS-1 and commercial Pt/C, (f) electrochemical stability test of Fe/NCNS-1 in 0.5 M H<sub>2</sub>SO<sub>4</sub>.

The electrocatalytic ORR performance of the Fe/NCNSs in 1 M KOH electrolyte was also investigated. The CV curves of Fe/NCNSs are shown in Figure S6. Distinct characteristic peaks were not also observed on the CV curves of Fe/NCNSs in the N<sub>2</sub>-saturated electrolyte, while the CV curves in the O<sub>2</sub>-saturated electrolyte all exhibited obvious cathodic peaks. LSV curves and the comparison of half-wave potential and  $j_k$  at 0.85 V are displayed in Figure 4a,b. Fe/NCNS-1 exhibited the best ORR activity with the half-wave potential of 0.865 V, more positive than that of commercial Pt/C (0.841 V), Fe/NCNS-2 (0.851 V) and Fe/NCNS-0 (0.753 V). The outstanding ORR activity of Fe/NCNS-1 is further confirmed with its high kinetic current density ( $j_k$ ) at 0.85 V (vs. RHE) of 22.3 mA·cm<sup>-2</sup>, which is 1.3 and 4.7 times those of Pt/C (17.1 mA·cm<sup>-2</sup>) and Fe/NCNS-0 (4.7 mA·cm<sup>-2</sup>),

respectively. In Figure 4c,  $n$  was calculated to be 3.51, 3.94, 3.92 for Fe/NCNS-0, Fe/NCNS-1 and Fe/NCNS-2, respectively, indicating their 4-electron-dominated electron transfer path in alkaline electrolytes.  $\text{H}_2\text{O}_2$  yield was 23%, 2% and 3% for Fe/NCNS-0, Fe/NCNS-1 and Fe/NCNS-2, respectively, and the electrochemical capacitances ( $C_{dl}$ ) were calculated to be 4.4, 6.5 and 5.4  $\text{mF cm}^{-2}$ , respectively (Figure S7). Furthermore, the Tafel slope values (141, 81, 87, and 95  $\text{mv}\cdot\text{dec}^{-1}$  for Fe/NCNS-0, Fe/NCNS-1, Fe/NCNS-2, and commercial Pt/C), respectively, in Figure 4d indicated the fastest kinetic rate of Fe/NCNS-1 during ORR in alkaline electrolyte. Besides, Fe/NCNS-1 also showed remarkable tolerance to methanol and electrochemical stability (Figure 4e,f). After the electrochemical stability test for 120 h, the current density still preserved about 90% of its initial current density. The results also suggested that Fe/NCNS-1 also possessed excellent ORR activity in alkaline electrolytes.

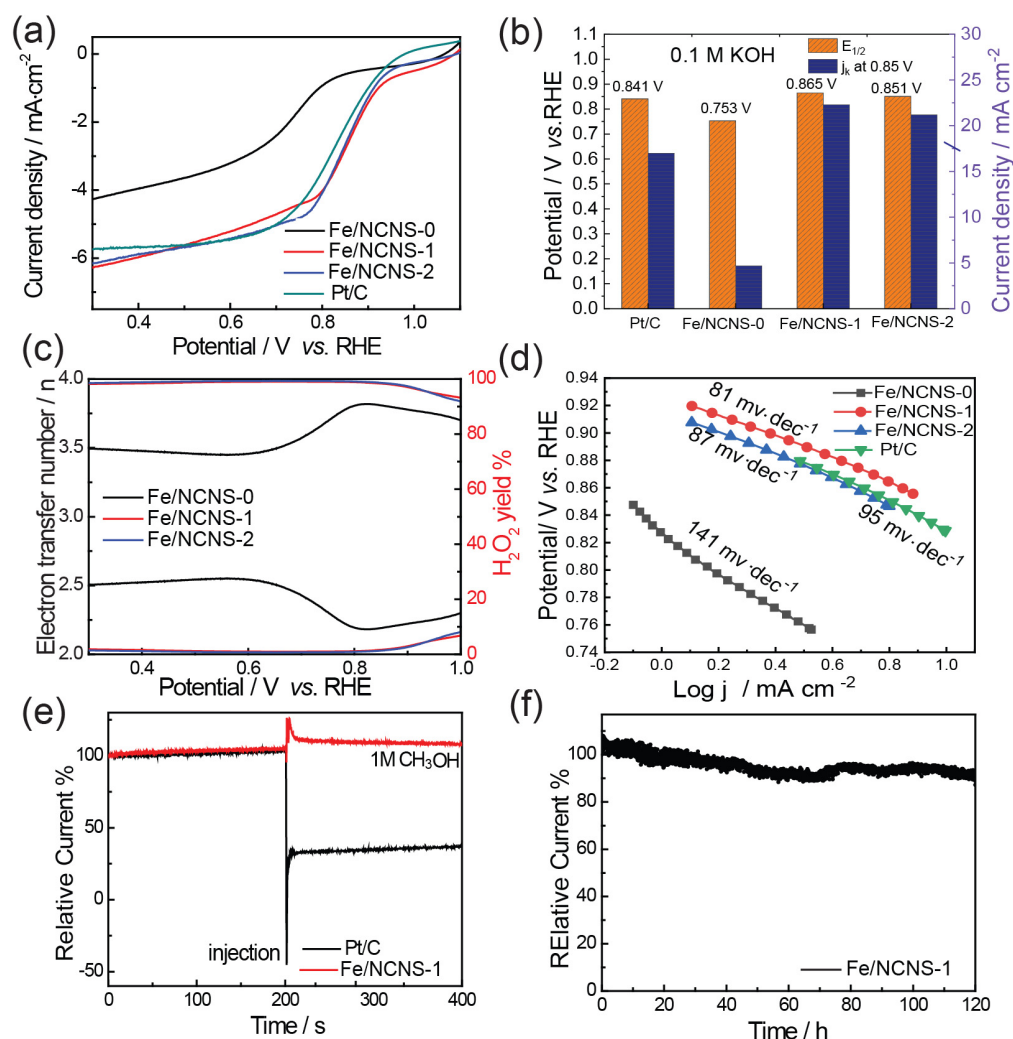


**Figure 4.** (a) LSV curves of Fe/NCNS-0, Fe/NCNS-1, Fe/NCNS-2 and commercial Pt/C at  $1600 \text{ rpm}\cdot\text{min}^{-1}$  in 0.1 M KOH; (b) comparison of  $j_k$  at 0.85 V and  $E_{1/2}$  of Fe/NCNS-0, Fe/NCNS-1, Fe/NCNS-2 and commercial Pt/C; (c) electron transfer number ( $n$ ) and the yield of  $\text{H}_2\text{O}_2$ ; (d) Tafel plots of Fe/NCNS-0, Fe/NCNS-1, Fe/NCNS-2 and commercial Pt/C; (e) the tolerance to methanol of Fe/NCNS-1 and commercial Pt/C, (f) electrochemical stability test of Fe/NCNS-1 in 0.1 M KOH.

The application of Fe/NCNS-1 as the air cathode in rechargeable ZABs was investigated. Figure 5a showed that the LED panel can be continuously powered by the prepared ZAB with Fe/NCNS-1 +  $\text{RuO}_2$  as the air cathode. The high open circuit voltage of 1.69 V was attributed to the excellent ORR performance of the Fe/NCNS-1. The discharge polarization curves and the corresponding power density of the ZAB were shown in Figure 5b.

The ZAB showed a higher discharge voltage at the same current density relative to ZAB with Pt/C + RuO<sub>2</sub> as the air cathode, suggesting its better rechargeability and energy efficiency. Furthermore, the peak power density was calculated on a basis of the discharge polarization curve for the batteries. Figure 5b indicated that ZAB with Fe/NCNS-1 + RuO<sub>2</sub> as the air cathode displayed a much higher power density of 1590 mW cm<sup>-2</sup> than ZAB with Pt/C + RuO<sub>2</sub> as the air cathode (1175 mW cm<sup>-2</sup>). The excellent catalytic performance in ZABs outperformed many reported Fe-N-C materials (Table S2). Figure 5c showed the cycling curves recorded at the constant current density of 5 mA cm<sup>-2</sup> with 10 min for each cycle. The charge/discharge voltage gap was 0.63 V at 5 mA cm<sup>-2</sup>. Further, the voltage gap increased by only 0.08 V after 300 cycles, suggesting the excellent charge/discharge cycling performance of the battery with Fe/NCNS-1 + RuO<sub>2</sub>, even under highly oxidative operating conditions in 6 M KOH.

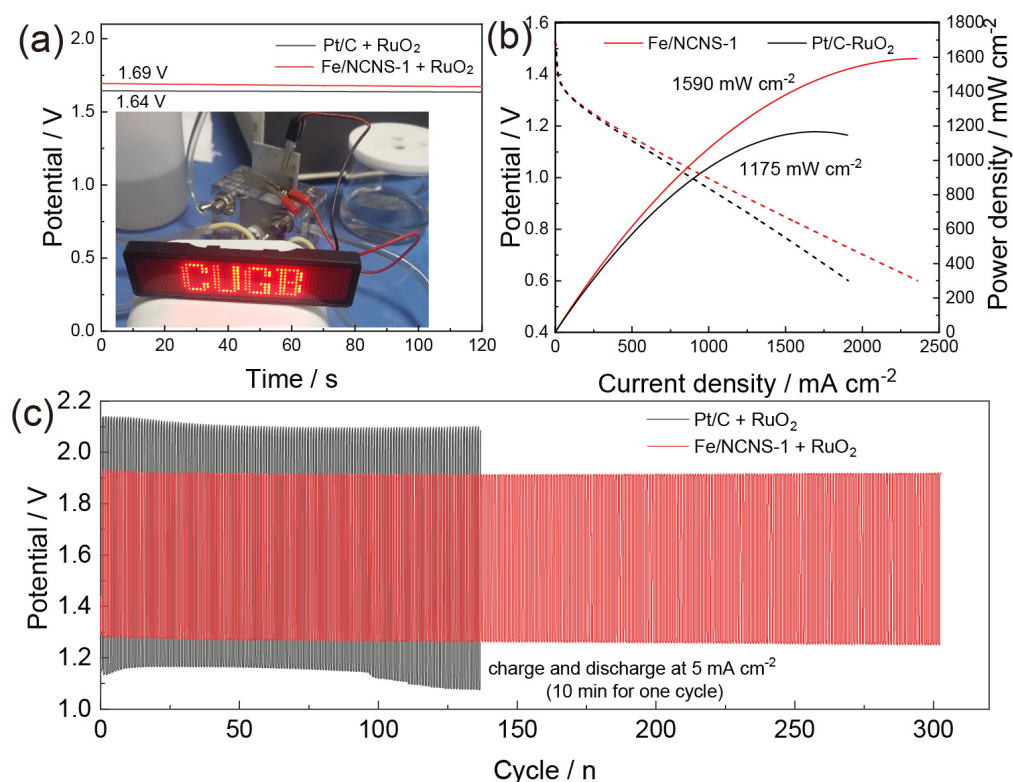


**Figure 5.** (a) Open circuit measurements for the Zn-air battery with Fe/NCNS-1 + RuO<sub>2</sub> and Pt/C + RuO<sub>2</sub> as air catalysts; (b) discharge polarization curves and the corresponding power density of the Zn-air batteries, (c) cycling stability of Fe/NCNS-1 + RuO<sub>2</sub> and Pt/C + RuO<sub>2</sub> at discharge/charge current densities of 5.0 mA cm<sup>-2</sup>.

### 3. Materials and Methods

#### 3.1. Synthesis of Fe/NCNSs

Typically, Fe/Zn dual-metal ZIFs (Fe/Zn-ZIFs) were prepared according to previously reported methods [31] with a slight modification. In brief, 0.1512 g ZnCl<sub>2</sub> and different amounts of FeCl<sub>3</sub>·6H<sub>2</sub>O (0.000 g, 0.0375 g or 0.0749 g) were dissolved in 40 mL of deionized (DI) water. Then, a 40 mL solution of 2-Methylimidazole (0.985 g) was added. The mixture was stirred vigorously for 24 h at room temperature. Fe/Zn-ZIFs were collected through centrifugation, washed with water and dried at 60 °C for 12 h. Fe/Zn-ZIFs with Fe/Zn ratios of 0:16, 1:16 and 2:16 were denoted as Fe/Zn-ZIF-0, Fe/Zn-ZIF-1 and Fe/Zn-ZIF-2. Fe/Zn-ZIFs were then carbonized at 900 °C for 2 h in a N<sub>2</sub> atmosphere. The obtained products were marked as Fe/NCNS-0, Fe/NCNS-1 and Fe/NCNS-2.

### 3.2. Preparation of Modified Electrodes

3 mg catalyst in 1.25 mL absolute ethanol was sonicated for 30 min to form a uniform dark ink. Then, 36  $\mu\text{L}$  of ink was coated on the prepolished rotating ring disk electrodes (RRDE, Shanghai, China, 4 mm in diameter) with a covering layer (6  $\mu\text{L}$ ) of Nafion (0.5 wt%, Alfa Aesar, Suzhou, China). The modified electrodes were dried at room temperature.

### 3.3. Electrochemical Measurement

All electrochemical tests were conducted using an electrochemical workstation (CHI 760E, Shanghai, China and Solartron 1287 & 1260, Shanghai, China) in 0.5 M  $\text{H}_2\text{SO}_4$  and 0.1 M KOH. The saturated Ag/AgCl electrode and graphite rod were used as a reference electrode and counter electrode, respectively. Cyclic voltammetry (CV, scan rate: 50  $\text{mV s}^{-1}$ ) and linear sweep voltammetry (LSV, scan rate: 10  $\text{mV s}^{-1}$ , rotating speed: 1600 rpm) were performed in  $\text{N}_2$ -saturated electrolyte and  $\text{O}_2$ -saturated electrolyte, respectively. Specifically, the potential of the platinum ring was fixed at 2.26 V in 0.5 M  $\text{H}_2\text{SO}_4$  and 1.46 V in 0.1 M KOH. The electrochemical stability was measured by the chronogalvanometry technique at 1.36 V and 0.66 V in acidic and alkaline media, respectively. Double-layer capacitance tests were performed at 5, 10, 20, 30, 40, and 50  $\text{mV s}^{-1}$  to evaluate their ECSA.

### 3.4. Zinc-Air Battery Tests

The zinc-air battery performance was evaluated in homemade cells. The air cathodes were constructed by dispersing the electrocatalysts, Fe/NCNS-1 and  $\text{RuO}_2$  (1:1 wt./wt.) or Pt/C and  $\text{RuO}_2$  (1:1 wt./wt.) on 1.5 cm  $\times$  5 cm carbon paper with a loading of 5.0  $\text{mg cm}^{-2}$ . Zinc foil was used as the anode. The electrolyte was a mixture of 6 M KOH and 0.2 M  $\text{Zn}(\text{Ac})_2 \cdot 2\text{H}_2\text{O}$ . Finally, the galvanostatic discharge cycles were recorded.

## 4. Conclusions

In summary, we synthesized Fe/NCNSs with the attractive morphology of two-dimensional nanosheets by simple calcination of Fe/Zn dual-metal ZIF-8 precursors, which are promising ORR catalysts in both acidic and alkaline electrolytes. Among them, Fe/NCNS-1 proved to be the most efficient ORR catalyst. Specifically, in 0.5 M  $\text{H}_2\text{SO}_4$ , the half-wave potential was determined to be 0.725 V, only 23 mV more negative than Pt/C (0.748 V). Meanwhile, in 0.1 M KOH, the value of the half-wave potential was 0.865 V, 24 mV more positive than commercial Pt/C (0.841 V). Fe/NCNS-1 showed excellent electrochemical stability in both media. The excellent performance of Fe/NCNS-1 in ORR was attributed to its highest specific surface area, ECSA and proportion of pyridinic N and Fe-N. Moreover, the rechargeable ZAB using Fe/NCNS-1 +  $\text{RuO}_2$  as an air electrode exhibited high power density (1590  $\text{mW cm}^{-2}$  at a current density of 2250  $\text{mA cm}^{-2}$ ), a low charge-discharge gap (0.63 V at 5  $\text{mA cm}^{-2}$ ) and long-term stability (over 300 cycles at 5  $\text{mA cm}^{-2}$ ). The work provides a strategy to fabricate two-dimensional efficient Fe-N-C-based electrocatalysts, helping pave the way for Zn-air batteries.

**Supplementary Materials:** The following supporting information can be downloaded at: <https://www.mdpi.com/article/10.3390/catal12101276/s1>, Figure S1: SEM images of Fe/Zn-ZIFs (a–c) and Fe/NCNS (d–f); Figure S2: XRD patterns of Fe/Zn-ZIF-0, Fe/Zn-ZIF-1 and Fe/Zn-ZIF-2; Figure S3: XPS spectra, O 1s spectra and C 1s spectra of Fe/NCNS-0 (a–c), Fe/NCNS-1 (d–f) and Fe/NCNS-2 (g–i); Figure S4: CV curves (scan rate: 50  $\text{mV} \cdot \text{s}^{-1}$ ) in  $\text{N}_2$  saturated (black dot line) and  $\text{O}_2$  saturated (solid line) 0.5 M  $\text{H}_2\text{SO}_4$ ; Figure S5: CV curves of Fe/NCNS-0 (a), Fe/NCNS-1 (b) and Fe/NCNS-2 (c) at 5, 10, 20, 30, 40, 50  $\text{mV} \cdot \text{s}^{-1}$  in 0.5 M  $\text{H}_2\text{SO}_4$  and corresponding correlation between the current density at 1.81 V and the scan rate (d); Figure S6: CV curves (scan rate: 50  $\text{mV} \cdot \text{s}^{-1}$ ) in  $\text{N}_2$  saturated (black dot line) and  $\text{O}_2$  saturated (solid line) 0.1 M KOH; Figure S7: CV curves of Fe/NCNS-0 (a), Fe/NCNS-1 (b) and Fe/NCNS-2 (c) at 5, 10, 20, 30, 40, 50  $\text{mV} \cdot \text{s}^{-1}$  in 0.1 M KOH and corresponding correlation between the current density at 1.31 V and the scan rate (d); Table S1: The comparison of ORR activity of Fe/NCNS-1 with reported Fe-based catalysts in acidic electrolyte [32–41]; Table S2: The comparison of Fe-N-C material electrocatalyst with reported in Zn-air batteries [15,18,19,42–46].

**Author Contributions:** Resources, X.L. (Xiaoming Liu); data curation, X.L. (Xiaoming Liu); writing—original draft preparation, X.W., W.X. and X.L. (Xiaoming Liu); writing—review and editing, X.L. (Xuanhe Liu) and Q.Z.; project administration, X.L. (Xiaoming Liu); funding acquisition, X.L. (Xiaoming Liu). All authors have read and agreed to the published version of the manuscript.

**Funding:** This work was supported by the National Natural Science Foundation of China (Grant No. 21603194) and the Fundamental Research Funds for the Central Universities (No. 2652018056 and 2652018004). Q.Z. acknowledges the support from the Hong Kong Postdoctoral Fellowship Scheme (HKUST PDFS2021-4S12).

**Data Availability Statement:** Not applicable.

**Acknowledgments:** We also thank the support from the large instruments and equipment sharing platform of the China University of Geosciences (Beijing).

**Conflicts of Interest:** The authors declare no conflict of interest.

## References

1. Ge, H.Y.; Li, G.D.; Shen, J.; Ma, W.; Meng, X.; Xu, L. Co<sub>4</sub>N nanoparticles encapsulated in N-doped carbon box as tri-functional catalyst for Zn-air battery and overall water splitting. *Appl. Catal. B* **2018**, *275*, 119104. [[CrossRef](#)]
2. Huang, L.B.; Zhao, L.; Zhang, Y.; Luo, H.; Zhang, X.; Zhang, J.; Pan, H.; Hu, J.S. Engineering carbon-shells of M@NC bifunctional oxygen electrocatalyst towards stable aqueous rechargeable Zn-air batteries. *Chem. Eng. J.* **2021**, *418*, 129409. [[CrossRef](#)]
3. Yu, X.; Zhou, T.; Ge, J.; Wu, C. Recent Advances on the Modulation of Electrocatalysts Based on Transition Metal Nitrides for the Rechargeable Zn-Air Battery. *ACS Appl. Mater. Interfaces* **2020**, *11*, 1423–1434. [[CrossRef](#)]
4. Jiang, S.; Suo, H.; Zhang, T.; Liao, C.; Wang, Y.; Zhao, Q.; Lai, W. Recent advances in seawater electrolysis. *Catalysts* **2022**, *12*, 123. [[CrossRef](#)]
5. Ji, Q.; Bi, L.; Zhang, J.; Cao, H.; Zhao, X.S. The role of oxygen vacancies of ABO<sub>3</sub> perovskite oxides in the oxygen reduction reaction. *Environ. Eng. Sci.* **2020**, *13*, 1408–1428. [[CrossRef](#)]
6. Tian, W.; Gao, Q.; Vahid Mohammadi, A.; Dang, J.; Li, Z.; Liang, X.; Hamed, M.M.; Zhang, L. Liquid-phase exfoliation of layered biochars into multifunctional heteroatom (Fe, N, S) Co-doped graphene-like carbon nanosheets. *Chem. Eng. J.* **2021**, *420*, 127601. [[CrossRef](#)]
7. Zhao, Q.; Wang, Y.; Lai, W.-H.; Xiao, F.; Lyu, Y.; Liao, C.; Shao, M. Approaching a high-rate and sustainable production of hydrogen peroxide: Oxygen reduction on Co–N–C single-atom electrocatalysts in simulated seawater. *Energy Environ. Sci.* **2021**, *14*, 5444–5456. [[CrossRef](#)]
8. Jorge, A.B.; Jervis, R.; Periasamy, A.P.; Qiao, M.; Feng, J.; Tran, L.N.; Titirici, M.M. 3D Carbon materials for efficient oxygen and hydrogen electrocatalysis. *Adv. Energy Mater.* **2020**, *10*, 1902494. [[CrossRef](#)]
9. Li, H.; Di, S.; Niu, P.; Wang, S.; Wang, J.; Li, L. A durable half-metallic diatomic catalyst for efficient oxygen reduction. *Energy Environ. Sci.* **2022**, *15*, 1601–1610. [[CrossRef](#)]
10. Xu, H.; Wang, D.; Yang, P.; Du, L.; Lu, X.; Li, R.; Liu, L.; Zhang, J.; An, M. A hierarchically porous Fe-N-C synthesized by dual melt-salt-mediated template as advanced electrocatalyst for efficient oxygen reduction in zinc-air battery. *Appl. Catal. B* **2022**, *305*, 121040. [[CrossRef](#)]
11. Liang, L.; Jin, H.; Zhou, H.; Liu, B.; Hu, C.; Chen, D.; Wang, Z.; Hu, Z.; Zhao, Y.; Li, H.W.; et al. Cobalt single atom site isolated Pt nanoparticles for efficient ORR and HER in acid media. *Nano* **2021**, *88*, 106221. [[CrossRef](#)]
12. Kong, F.; Cui, X.; Huang, Y.; Yao, H.; Chen, Y.; Tian, H.; Meng, G.; Chen, C.; Chang, Z.; Shi, J. N-Doped carbon electrocatalyst: Marked ORR activity in acidic media without the contribution from metal sites? *Angew. Chem. Int. Ed.* **2022**, *61*, 15. [[CrossRef](#)]
13. Zhang, B.; Qi, Z.; Wu, Z.; Lui, Y.H.; Kim, T.-H.; Tang, X.; Zhou, L.; Huang, W.; Hu, S. Defect-rich 2D material networks for advanced oxygen evolution catalysts. *ACS Energy Lett.* **2018**, *41*, 328–336. [[CrossRef](#)]
14. Guan, Y.; Li, Y.; Luo, S.; Ren, X.; Deng, L.; Sun, L.; Mi, H.; Zhang, P.; Liu, J. Rational design of positive-hexagon-shaped two-dimensional ZIF-derived materials as improved bifunctional oxygen electrocatalysts for use as long-lasting rechargeable Zn-Air batteries. *Appl. Catal. B* **2019**, *256*, 117923. [[CrossRef](#)]
15. Wu, G.; Shao, C.; Cui, B.; Chu, H.; Qiu, S.; Zou, Y.; Xu, F.; Sun, L. Honeycomb-like Fe/Fe<sub>3</sub>C-doped porous carbon with more Fe-N<sub>x</sub> active sites for promoting the electrocatalytic activity of oxygen reduction. *Sustain. Energy Fuels* **2021**, *520*, 5295–5304. [[CrossRef](#)]
16. Luo, M.; Ortiz, A.L.; Shaw, L.L. Enhancing the electrochemical performance of NaCrO<sub>2</sub> through structural defect control. *ACS Appl. Energy Mater.* **2020**, *3*, 7216–7227. [[CrossRef](#)]
17. Yang, L.; Zhang, X.; Yu, L.; Hou, J.; Zhou, Z.; Lv, R. Edge-site engineering of atomically dispersed Fe-N<sub>4</sub> by selective C-N bond cleavage for enhanced ORR activities. *J. Am. Chem. Soc.* **2018**, *140*, 11594–11598.
18. Zhu, Y.; Wang, X.; Shi, J.; Gan, L.; Huang, B.; Tao, L.; Wang, S. Neuron-inspired design of hierarchically porous carbon networks embedded with single-iron sites for efficient oxygen reduction. *Sci. China Chem.* **2022**, *657*, 1445–1452. [[CrossRef](#)]

19. Fang, J.; Zhang, X.; Wang, X.; Liu, D.; Xue, Y.; Xu, Z.; Zhang, Y.; Song, C.; Zhu, W.; Zhuang, Z. A metal and nitrogen doped carbon composite with both oxygen reduction and evolution active sites for rechargeable zinc–air batteries. *J. Mater. Chem. A* **2020**, *831*, 15752–15759. [[CrossRef](#)]
20. Sun, Z.; Wang, Y.; Zhang, L.; Wu, H.; Jin, Y.; Li, Y.; Shi, Y.; Zhu, T.; Mao, H.; Liu, J.; et al. Simultaneously realizing rapid electron transfer and mass transport in jellyfish-like Mott–Schottky nanoreactors for oxygen reduction reaction. *Adv. Mater.* **2020**, *3015*, 1910482. [[CrossRef](#)]
21. Hu, C.; Jin, H.; Liu, B.; Liang, L.; Wang, Z.; Chen, D.; He, D.; Mu, S. Propagating Fe-N<sub>4</sub> active sites with vitamin C to efficiently drive oxygen electrocatalysis. *Nano* **2021**, *82*, 105714. [[CrossRef](#)]
22. Wang, Y.; Wu, M.; Wang, K.; Chen, J.; Yu, T.; Song, S. Fe<sub>3</sub>O<sub>4</sub>@N-Doped Interconnected hierarchical porous carbon and its 3D integrated electrode for oxygen reduction in acidic media. *Adv. Sci.* **2020**, *7*, 2000407. [[CrossRef](#)] [[PubMed](#)]
23. Zhang, T.; Bian, J.; Zhu, Y.; Sun, C. FeCo Nanoparticles encapsulated in N-doped carbon nanotubes coupled with layered double (Co, Fe) hydroxide as an efficient bifunctional catalyst for rechargeable zinc-air batteries. *Small* **2021**, *17*, 2103737. [[CrossRef](#)] [[PubMed](#)]
24. Kordek, K.; Jiang, L.; Fan, K.; Zhu, Z.; Xu, L.; Al-Mamun, M.; Dou, Y.; Chen, S.; Liu, P.; Yin, H.; et al. Two-step activated carbon cloth with oxygen-rich functional groups as a high-performance additive-free air electrode for flexible zinc-air batteries. *Adv. Energy Mater.* **2019**, *9*, 1802936. [[CrossRef](#)]
25. Luo, X.; Wei, X.; Wang, H.; Gu, W.; Kaneko, T.; Yoshida, Y.; Zhao, X.; Zhu, C. Secondary-atom-doping enables robust Fe-N-C single-atom catalysts with enhanced oxygen reduction reaction. *Nanomicro. Lett.* **2020**, *12*, 163. [[CrossRef](#)]
26. Wang, J.; Liu, W.; Luo, G.; Li, Z.; Zhao, C.; Zhang, H.; Zhu, M.; Xu, Q.; Wang, X.; Zhao, C.; et al. Synergistic effect of well-defined dual sites boosting the oxygen reduction reaction. *Energy Environ. Sci.* **2018**, *11*, 3375–3379. [[CrossRef](#)]
27. Su, Y.; Li, C.; Yao, C.; Xu, L.; Xue, J.; Yuan, W.; Liu, J.; Cheng, M.; Hou, S. Palladium nanoparticles immobilized in B, N doped porous carbon as electrocatalyst for ethanol oxidation reaction. *Mater. Today Energy* **2021**, *20*, 100628. [[CrossRef](#)]
28. Liu, D.; Li, J.C.; Ding, S.; Lu, Z.; Feng, S.; Tian, H.; Huyan, C.; Xu, M.; Li, T.; Du, D.; et al. 2D Single-atom catalyst with optimized iron sites produced by thermal melting of metal-organic frameworks for oxygen reduction reaction. *Small Methods* **2020**, *4*, 1900827. [[CrossRef](#)]
29. Tang, C.; Chen, L.; Li, H.; Li, L.; Jiao, Y.; Zheng, Y.; Xu, H.; Davey, K.; Qiao, S.Z. Tailoring acidic oxygen reduction selectivity on single-atom catalysts via modification of first and second coordination spheres. *J. Am. Chem. Soc.* **2021**, *143*, 7819–7827. [[CrossRef](#)] [[PubMed](#)]
30. Wang, Z.; Jin, X.; Zhu, C.; Liu, Y.; Tan, H.; Ku, R.; Zhang, Y.; Zhou, L.; Liu, Z.; Hang, S.J.; et al. Atomically dispersed Co<sub>2</sub>-N<sub>6</sub> and Fe-N<sub>4</sub> costructures boost oxygen reduction reaction in both alkaline and acidic media. *Adv. Mater.* **2021**, *33*, 2104718. [[CrossRef](#)]
31. Fu, X.; Gao, R.; Jiang, G.; Li, M.; Li, S.; Luo, D.; Hu, Y.; Yuan, Q.; Huang, W.; Zhu, N.; et al. Evolution of atomic-scale dispersion of FeN<sub>x</sub> in hierarchically porous 3D air electrode to boost the interfacial electrocatalysis of oxygen reduction in PEMFC. *Nano* **2021**, *83*, 105734. [[CrossRef](#)]
32. Zhang, N.; Zhou, T.; Chen, M.; Feng, H.; Yuan, R.; Zhong, C.A.; Yan, W.; Tian, Y.; Wu, X.; Chu, W.; et al. High-purity pyrrole-type FeN<sub>4</sub> sites as a superior oxygen reduction electrocatalyst. *Energy Environ. Sci.* **2020**, *13*, 111–118. [[CrossRef](#)]
33. Zhang, Z.; Sun, J.; Wang, F.; Dai, L. Efficient oxygen reduction reaction (ORR) catalysts based on single iron atoms dispersed on a hierarchically structured porous carbon framework. *Angew. Chem. Int. Ed. Engl.* **2018**, *57*, 9038–9043. [[CrossRef](#)]
34. Yi, J.D.; Xu, R.; Wu, Q.; Zhang, T.; Zang, K.T.; Luo, J.; Liang, Y.L.; Huang, Y.B.; Cao, R. Atomically dispersed iron–nitrogen active sites within porphyrinic triazine-based frameworks for oxygen reduction reaction in both alkaline and acidic media. *ACS Energy Lett.* **2018**, *3*, 883–889. [[CrossRef](#)]
35. Qiao, M.; Wang, Y.; Wang, Q.; Hu, G.; Mamat, X.; Zhang, S.; Wang, S. Hierarchically ordered porous carbon with atomically dispersed FeN<sub>4</sub> for ultraefficient oxygen reduction reaction in proton-exchange membrane fuel cells. *Angew. Chem. Int. Ed.* **2020**, *59*, 2688–2694. [[CrossRef](#)] [[PubMed](#)]
36. Chen, X.; Wang, N.; Shen, K.; Xie, Y.; Tan, Y.; Li, Y. Mof-derived isolated Fe atoms implanted in N-doped 3D hierarchical carbon as an efficient ORR electrocatalyst in both alkaline and acidic media. *ACS Appl. Mater. Interfaces* **2019**, *11*, 25976–25985. [[CrossRef](#)]
37. Huo, L.L.; Liu, B.C.; Zhang, G.; Zhang, J. 2D Layered non-precious metal mesoporous electrocatalysts for enhanced oxygen reduction reaction. *J. Mater. Chem. A* **2017**, *5*, 4868–4878. [[CrossRef](#)]
38. Qiao, M.; Wang, Y.; Mamat, X.; Chen, A.; Zou, G.; Li, L.; Hu, G.; Zhang, S.; Hu, X.; Voiry, D. Rational design of hierarchical, porous, Co-supported, N-doped carbon architectures as electrocatalyst for oxygen reduction. *ChemSusChem* **2020**, *13*, 741–748. [[CrossRef](#)] [[PubMed](#)]
39. Qian, Y.; Liu, Q.; Sarnello, E.; Tang, C.; Chng, M.; Shui, J.; Li, T.; Pennycook, S.J.; Han, M.; Zhao, D. Mof-derived carbon networks with atomically dispersed Fe–N<sub>x</sub> sites for oxygen reduction reaction catalysis in acidic media. *ACS Appl. Mater. Interfaces* **2019**, *1*, 37–43. [[CrossRef](#)]
40. Deng, Y.; Chi, B.; Tian, X.; Cui, Z.; Liu, E.; Jia, Q.; Fan, W.; Wang, G.; Dang, D.; Li, M.; et al. g-C<sub>3</sub>N<sub>4</sub> promoted mof derived hollow carbon nanopolyhedra doped with high density/fraction of single Fe atoms as an ultra-high performance non-precious catalyst towards acidic ORR and PEM fuel cells. *J. Mater. Chem. A* **2019**, *7*, 5020–5030. [[CrossRef](#)]
41. Liu, X.; Liu, H.; Chen, C.; Zou, L.; Li, Y.; Zhang, Q.; Yang, B.; Zou, Z.; Yang, H. Fe<sub>2</sub>N nanoparticles boosting FeN<sub>x</sub> moieties for highly efficient oxygen reduction reaction in Fe-N-C porous catalyst. *J. Nano Res.* **2019**, *12*, 1651–1657. [[CrossRef](#)]

42. Zhu, Z.-H.; Yu, B.; Sun, W.; Chen, S.; Wang, Y.; Li, X.; Lv, L.P. Triazine organic framework derived Fe single-atom bifunctional electrocatalyst for high performance zinc air batteries. *J. Power Sources* **2022**, *542*, 231583. [[CrossRef](#)]
43. Wang, W.; Rui, K.; Wu, K.; Wang, Y.; Ke, L.; Wang, X.; Xu, F.; Lu, Y.; Zhu, J. Molecular Bridging Enables Isolated Iron Atoms on Stereoassembled Carbon Framework to Boost Oxygen Reduction for Zinc-Air Batteries. *Chemistry* **2022**, *2840*, e202200789. [[CrossRef](#)] [[PubMed](#)]
44. Sheng, J.; Sun, S.; Jia, G.; Zhu, S.; Li, Y. Doping Effect on Mesoporous Carbon-Supported Single-Site Bifunctional Catalyst for Zinc-Air Batteries. *ACS Nano* **2022**, *in press*. [[CrossRef](#)] [[PubMed](#)]
45. Wu, D.; Hu, X.; Yang, Z.; Yang, T.; Wen, J.; Lu, G.; Zhao, Q.; Li, Z.; Jiang, X.; Xu, C. NiFe LDH Anchoring on Fe/N-Doped Carbon Nanofibers as a Bifunctional Electrocatalyst for Rechargeable Zinc–Air Batteries. *Ind. Eng. Chem. Res.* **2022**, *6122*, 7523–7528. [[CrossRef](#)]
46. Zhou, F.; Yu, P.; Sun, F.; Zhang, G.; Liu, X.; Wang, L. The cooperation of Fe<sub>3</sub>C nanoparticles with isolated single iron atoms to boost the oxygen reduction reaction for Zn-air batteries. *J. Mater. Chem. A* **2021**, *911*, 6831–6840. [[CrossRef](#)]